Check for updates

View Article Online
View Journal

Chemical
Science

Accepted Manuscript

This article can be cited before page numbers have been issued, to do this please use: Y. Ishii, C. Hanafusa, H. Suzuki, D. Kato, O. Tomita, A. Nakada, S. Nozawa, A. Saeki and R. Abe, *Chem. Sci.*, 2026, DOI: 10.1039/D6SC02806C.

ROYAL SOCIETY OF CHEMISTRY

rsc.li/chemical-science

View Article Online
DOI: 10.1039/D6SC02806C

ARTICLE

Received 00th January 20xx,
Accepted 00th January 20xx

DOI: 10.1039/x0xx00000x

Design of active interlayer space in layered oxysulfide photocatalysts $NaMTiO_{2.2}S_{1.8}$ (M = lanthanoid) for efficient visible light hydrogen evolution

Yusuke Ishii,[a] Chisato Hanafusa,[a] Hajime Suzuki,*[a,b] Daichi Kato,[a] Osamu Tomita,[a] Akinobu Nakada,[a] Shunsuke Nozawa,[c] Akinori Saeki,[d] Ryu Abe*[a]

Interlayer-active layered oxysulfides, which exhibit both interlayer hydration and ion-exchange capabilities, have recently emerged as a new class of visible-light-driven photocatalysts for water splitting. However, the utilization of interlayer galleries as reaction fields remains unexplored in oxysulfide photocatalysts. Here we demonstrate the interlayer space of a layered oxysulfide as an active reaction field for H_2 evolution. Interlayer-active layered oxysulfides $NaMTiO_{2.2}S_{1.8}$ (M = Pr, Nd, Sm, Eu, and Gd) were synthesized *via* a solid-state reaction, yielding submicrometer-sized particles suitable for effective utilization of the interlayer space, markedly smaller than those obtained by the previous H_2S-based method. Ni species were introduced into the active interlayer *via* ion-exchange with interlayer Na^+. The interlayer-Ni-loaded $NaMTiO_{2.2}S_{1.8}$ exhibits significantly enhanced H_2 evolution activity compared with surface-Ni-loaded $NaMTiO_{2.2}S_{1.8}$, owing to more efficient utilization of photogenerated electrons within the particle interior. These results provide a new design concept for layered oxysulfide photocatalysts toward efficient visible-light-driven water splitting.

Introduction

Layered oxides that can utilize their interlayer space as reaction sites for guest molecular intercalation or interlayer ion-exchange have attracted considerable attention in various fields,[1–5] including (photo)catalysis,[6–11] batteries,[12–14] adsorbents,[15–17] and solid electrolytes.[18–20] These oxides (*e.g.*, $K_4Nb_6O_{17}$) basically consist of anionic oxide nanosheets and interlayer cations (*e.g.*, Na^+ and K^+). This host–guest architecture enables the reversible accommodation and exchange of a wide variety of ions and molecules within the interlayer galleries, which underpins its diverse applications. In photocatalysis, "interlayer-active" layered oxide semiconductors, which can coordinate water molecules to interlayer cations and exchange these cations with alternative species have been extensively investigated. Owing to this ion-exchange capability, the interlayer cations can be replaced by other cations (*e.g.*, Ni and Pt cation species), thereby incorporating metallic cocatalysts into the interlayer space to promote H_2 evolution.[9,21,22] In such "interlayer-active" materials, photogenerated charge carriers should migrate only 1–2 nm across the oxide layer to react with interlayer water molecules, eventually suppressing charge recombination. Indeed, some "interlayer-active" layered oxides (*e.g.*, $K_4Nb_6O_{17}$,[9,21] $K_2La_2Ti_3O_{10}$,[8,10] and $NaLaTa_2O_7$[23]) exhibit efficient overall water splitting under ultraviolet (UV) light irradiation. However, their wide bandgaps limit the utilization of visible light that constitutes the majority of the solar spectrum. This issue is basically caused by excessively positive level of valence band maximum (VBM), generally at around +3.0 V vs. standard hydrogen electrode (SHE), derived solely from O-2p orbitals.[24]

Recently, we successfully synthesized novel "interlayer-active" layered oxysulfides, $NaMTiO_{2.2}S_{1.8}$ (M = Nd and Sm) (Fig. 1a) by heating the layered oxide $NaMTiO_4$ precursor under a H_2S flow at a high temperature.[25] $NaMTiO_{2.2}S_{1.8}$ features an n = 1 Ruddlesden–Popper structure with both interlayer hydration and ion-exchange capabilities. The upper parts of valence bands in the oxysulfides are primarily composed of S-3p orbitals with additional contributions from the O-2p orbitals, which elevate the VBM and thereby decrease the bandgaps compared to the corresponding oxides. In particular, $NaMTiO_{2.2}S_{1.8}$ represents the first example of an "interlayer-active" layered oxysulfide that exhibits both H_2 and O_2 evolution under visible light irradiation. Nevertheless, despite its hydration nature, the utilization of the interlayer space as water splitting reaction field has remained unachieved.

In this study, we demonstrate efficient photocatalytic H_2 evolution by enabling the interlayer space to function as a water reduction site through particle design of the "interlayer-active" layered oxysulfide $NaMTiO_{2.2}S_{1.8}$ (M = lanthanoid). Nearly single-phase $NaMTiO_{2.2}S_{1.8}$ (M = La, Pr, Nd, Sm, Eu, and Gd)

---

[a] Department of Energy and Hydrocarbon Chemistry, Graduate School of Engineering, Kyoto University, Nishikyo-ku, Kyoto 615-8510, Japan
[b] Precursory Research for Embryonic Science and Technology (PRESTO), Japan Science and Technology Agency (JST), 4-1-8 Honcho, Kawaguchi, Saitama 332-0012, Japan
[c] Photon Factory (PF), Institute of Materials Structure Science (IMSS), High Energy Accelerator Research Organization (KEK), Tsukuba, Ibaraki 305-0801, Japan
[d] Department of Applied Chemistry, Graduate School of Engineering, Osaka University, 2-1 Yamadaoka, Suita, Osaka 565-0871, Japan

View Article Online
DOI: 10.1039/D5SC08806C

samples were first synthesized *via* an H_2S-free solid-state reaction (SSR) at lower calcination temperatures. This approach resulted in smaller particle sizes (~several hundred nanometers) than those obtained by the previous H_2S-based method, which is advantageous for the effective utilization of the interlayer space. Subsequently, Ni species in the form of $[Ni(H_2O)_x]^{2+}$ were successfully introduced into the interlayer of $NaMTiO_{2.2}S_{1.8}$ *via* ion-exchange with Na^+. The obtained interlayer-Ni-loaded $NaGdTiO_{2.2}S_{1.8}$ exhibited higher H_2 evolution activity than both other interlayer-Ni-loaded $NaMTiO_{2.2}S_{1.8}$ and surface-Ni-loaded $NaGdTiO_{2.2}S_{1.8}$, owing to efficient electron transfer to the interlayer Ni species. To the best of our knowledge, this study represents the first demonstration of photocatalytic H_2 evolution using the interlayer space of a layered oxysulfide photocatalyst as reaction sites.

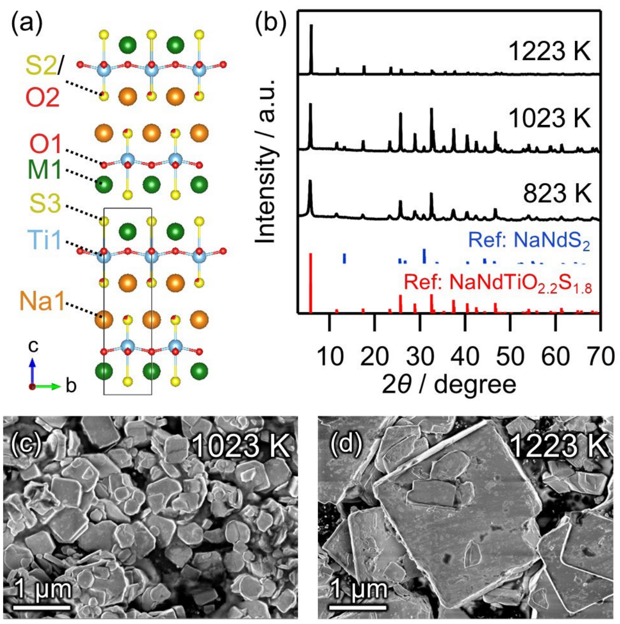

Fig. 1 (a) Crystal structure of $NaMTiO_{2.2}S_{1.8}$ (M = Nd and Sm). (b-d) XRD patterns and SEM images of $NaNdTiO_{2.2}S_{1.8}$ obtained *via* solid-state reaction (SSR) at 823, 1023 and 1223 K, along with reference patterns of $NaNdTiO_{2.2}S_{1.8}$ (previous study[25]) and $NaNdS_2$ (ICSD #644913).

Results and discussion

Solid-state synthesis of layered oxysulfide $NaNdTiO_{2.2}S_{1.8}$ without using H_2S.

Focusing on $NaNdTiO_{2.2}S_{1.8}$, which exhibited the highest H_2 evolution activity in our previous study,[25] we first conducted solid-state synthesis at 1223 K under vacuum using various precursor combinations (Fig. S1). Among these, the combination of Na_2CO_3, Nd_2O_3, and TiS_2 yielded $NaNdTiO_{2.2}S_{1.8}$ with the highest phase purity. Subsequently, solid-state synthesis was conducted using these precursors at various temperatures (723–1323 K) (Figs. 1b and S2). $NaNdTiO_{2.2}S_{1.8}$ was obtained almost as a single phase at 823–1323 K. Scanning electron microscopy (SEM) images revealed that particle size increased with calcination temperature, and coarse particles on the order of several micrometers were observed at 1223 K, similar to those produced by the H_2S method (Figs. 1c and S3). In contrast, lower temperatures (823 and 1023 K) yielded relatively smaller particles on the order of several hundred nanometers (Figs. 1d and S3). Next, Rh was photo-deposited onto the obtained photocatalysts, and their H_2 evolution activities were evaluated in the presence of sacrificial electron donors (*i.e.*, S^{2-} and SO_3^{2-}) (Fig. S4). The photocatalysts synthesized at 1023, 1123, and 1223 K exhibited higher activities than those obtained at the other temperatures (see discussion in Fig. S5 and Table S1). Notably, the sample synthesized at 1023 K combined high activity with a small particle size, making it particularly promising for loading cocatalysts into the interlayer, as discussed later.

Solid-state synthesis of layered oxysulfide $NaMTiO_{2.2}S_{1.8}$ (M = La, Pr, Sm, Eu, and Gd).

Because $NaNdTiO_{2.2}S_{1.8}$, synthesized at 1023 K, exhibited both high photocatalytic activity and a small particle size, the solid-state synthesis of $NaMTiO_{2.2}S_{1.8}$ (M = La, Pr, Sm, Eu, Gd, and Y) was conducted using Na_2CO_3, M_2O_3, and TiS_2 as precursors at 1023 K (Fig. 2). For M = Sm, the product was obtained as an almost single phase of $NaSmTiO_{2.2}S_{1.8}$, similar to that obtained by the previous H_2S-based method.[25] In contrast, the X-ray diffraction (XRD) patterns of the products with M = La, Pr, Eu, and Gd showed main peaks analogous to those of $NaNdTiO_{2.2}S_{1.8}$ (Fig. S6). Notably, for M = Y, $Y_2Ti_2O_7$ and $NaYS_2$ were detected as impurity phases, consistent with the previous report,[25] suggesting that $NaYTiO_{2.2}S_{1.8}$ is thermodynamically unstable. The particle sizes of the products were on the order of several hundred nanometers, comparable to that of $NaNdTiO_{2.2}S_{1.8}$, although the sample with M = Eu exhibited slightly larger particles (Fig. S7). Then, Rietveld refinements of the synchrotron X-ray powder diffraction (SXRPD) data of the samples with M = La, Pr, Eu, and Gd synthesized at 1023 K were performed using the previously reported crystal structure of $NaMTiO_{2.2}S_{1.8}$ (M = Nd and Sm). All refinements yielded good fits (Fig. S8) with the reliability factors (M = La: R_{wp} = 6.06 % and GOF = 1.41; M = Pr: R_{wp} = 8.20 % and GOF = 1.99; M = Eu: R_{wp} =

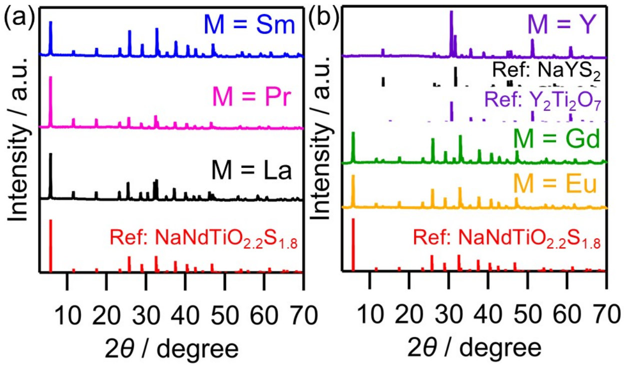

Fig. 2 XRD patterns of the samples (M = (a) La, Pr, Sm and (b) Eu, Gd, Y) obtained *via* SSR at 1023 K, along with reference patterns of $NaNdTiO_{2.2}S_{1.8}$ (previous study), $Y_2Ti_2O_7$ (ICSD #66874), and $NaYS_2$ (ICSD #195944).

View Article Online
DOI: 10.1039/D6SC02806C

9.90 % and GOF = 1.48; M = Gd: R_{wp} = 6.71 % and GOF = 1.34). The obtained crystal structures and crystallographic parameters are shown in Fig. S9 and Tables S2–S5, respectively. In the $NaMTiO_{2.2}S_{1.8}$ structure, the S3 site is fully occupied by sulfur, while the S2 site exhibits mixed sulfur/oxygen occupancy of approximately 80/20. These compositions are in good agreement with the energy-dispersive X-ray spectroscopy (EDX) results showing similar elemental ratios (Na/Ti ≈ 0.9–1, M/Ti ≈ 1–1.1, S/Ti ≈ 1.6–1.7) (Table S6). These results demonstrate that the SSR method developed in this study can form $NaMTiO_{2.2}S_{1.8}$ as the major phase for wider range of lanthanoids, including La, Pr, Eu, and Gd, for which the previous H_2S method fails to produce this phase as the primary product for them.

Next, we investigated the ion-exchange and interlayer hydration capabilities (*i.e.*, “interlayer-active” behaviour) of $NaMTiO_{2.2}S_{1.8}$ synthesized *via* the SSR method. To evaluate these properties, the samples were immersed in an H_2SO_4 aqueous solution (pH = 2.5) for 1 h (Figs. 3a and S10). The (001) peak of the $NaLaTiO_{2.2}S_{1.8}$ sample showed no discernible shift after immersion (Fig. 3a). In contrast, all other samples exhibited a clear shift toward lower angles, consistent with previously reported behaviour for $NaNdTiO_{2.2}S_{1.8}$ and $NaSmTiO_{2.2}S_{1.8}$ (Fig. S10). Such peak shifts are attributed to an expansion of the *c*-axis lattice parameter due to the intercalation of water molecules in the interlayer space, indicating that the M = Pr, Eu, and Gd samples possess interlayer hydration capability. Then, the Na/Ti ratios before and after the immersion were compared by EDX analysis. All samples, including M = La, showed a substantial decrease in the Na/Ti ratios after the immersion (M = La: before ≈ 0.9, after ≈ 0.5; M = Pr, Eu, Gd: before ≈ 0.9–1.0, after ≈ 0.1–0.2), indicating that all $NaMTiO_{2.2}S_{1.8}$ samples possess proton exchange capability (Table S7). This difference in interlayer hydration capability among the $NaMTiO_{2.2}S_{1.8}$ samples may be related to variations in the charge density of the oxysulfide layers, which depend on the ionic radius of M^{3+}. The interlayer hydration amounts, *n*, in the oxysulfides, estimated from thermogravimetric-differential thermal analysis (TG-DTA), ranged from 0.1 to 0.4 depending on M (see Tables S7, S8, and Fig. S11 for details). These results demonstrate that $NaMTiO_{2.2}S_{1.8}$ with M = Pr, Eu, and Gd, in addition to the previously reported cases with M = Nd and Sm, is also an “interlayer-active” layered oxysulfide.

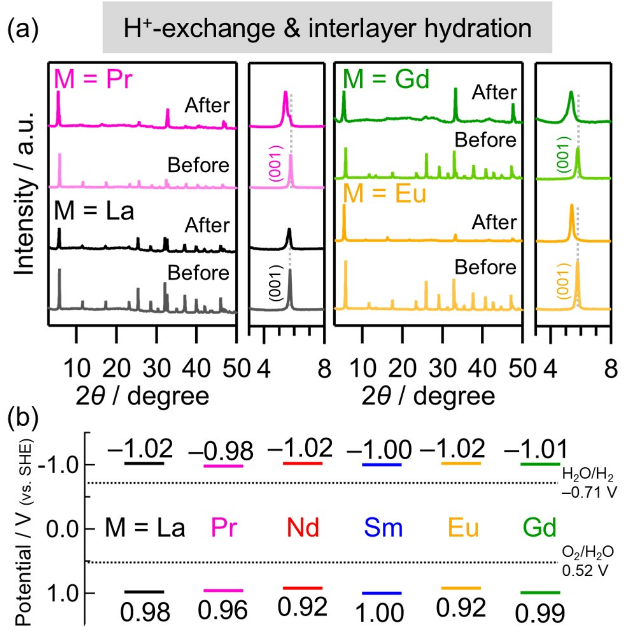

Fig. 3 (a) XRD patterns of $NaMTiO_{2.2}S_{1.8}$ (M = La, Pr, Eu, and Gd) obtained *via* SSR at 1023 K before and after immersion in an H_2SO_4 aqueous solution for 1 h under dark condition. (b) Band levels at pH =12 of $NaMTiO_{2.2}S_{1.8}$.

Wavelength-dependent time-resolved microwave conductivity (TRMC) measurements[26,27] and Mott-Schottky (MS) plots were performed to evaluate the band positions of $NaMTiO_{2.2}S_{1.8}$ (Fig. 3b). Because these oxysulfides contain lanthanoid ions, which generate additional absorption features due to localized f–f transitions, their bandgaps are difficult to determine unambiguously from diffuse reflectance spectra. Therefore, TRMC, which detects signals arising from mobile charge carriers, was employed to determine the effective bandgaps. The wavelength-dependent spectra for $NaMTiO_{2.2}S_{1.8}$ were recorded with excitation wavelengths in the range of 355–660 nm (Figs. S12 and S13). The TRMC action spectra showed that all samples were photoresponsive up to approximately 600 nm, and the onset of the TRMC signal closely matched the absorption edge observed in the diffuse reflectance spectra. The band positions of $NaMTiO_{2.2}S_{1.8}$ were subsequently determined from a combination of the effective bandgap estimated from TRMC and the flat-band potential estimated from the MS plots (Fig. S14). Given that $NaMTiO_{2.2}S_{1.8}$ behaves as an n-type semiconductor, the flat-band potential is approximated to lie just below the conduction band minimum. As shown in Fig. 3b, all $NaMTiO_{2.2}S_{1.8}$ samples exhibit band positions are thermodynamically appropriate for both water reduction and oxidation under visible light irradiation. These results demonstrate that $NaMTiO_{2.2}S_{1.8}$ with M = Pr, Eu, and Gd, in addition to the previously reported M = Nd and Sm analogues, demonstrate visible light absorption capability, “interlayer-active” characteristics, and band positions suitable for overall water splitting.

Utilization of interlayer space in $NaMTiO_{2.2}S_{1.8}$ as water reduction sites.

The interlayer Na^+ in $NaMTiO_{2.2}S_{1.8}$ synthesized *via* SSR at 1023 K was ion-exchanged with Ni cation species, based on the previously reported ion-exchange method for the layered oxide $K_4Nb_6O_{10}$.[9,22,28] $NaMTiO_{2.2}S_{1.8}$ was immersed in an aqueous solution of $Ni(NO_3)_2$ (0.5 wt% as Ni metal) for 24 h for the ion-exchange, and the resulting sample is denoted as Ni(in)/$NaMTiO_{2.2}S_{1.8}$. The photocatalytic H_2 evolution activities of Ni(in)/$NaMTiO_{2.2}S_{1.8}$ are shown in Fig. 4a and Fig. S15. All samples except M = La showed steady H_2 evolution under visible-light irradiation, with the activity increasing in the order M = Eu < Nd < Sm < Pr < Gd. Note that the corresponding oxides exhibit no photocatalytic activity under visible light[25] (see also Fig. S16 for a representative comparison). Consistent with this

View Article Online
DOI: 10.1039/D6SC02806C

observation, the XRD patterns of all samples except M = La remained largely unchanged after the photocatalytic reactions, indicating that these oxysulfides functioned as stable photocatalysts (Fig. S17). In contrast, the M = La sample displayed a pronounced increase in the diffraction peaks corresponding to the oxide $Na_{0.5}La_{0.5}TiO_3$ (a similar trend was also observed for Rh(out)/$NaLaTiO_{2.2}S_{1.8}$), demonstrating that $NaLaTiO_{2.2}S_{1.8}$ is not stable as a photocatalyst (Fig. S18). Fig. 4b compares the H_2 evolution amount after 5 h for Ni(in)/$NaMTiO_{2.2}S_{1.8}$ with the maximum photoconductivity ($\Delta\sigma_{max}$) obtained from TRMC measurements (excitation at 500 nm) for $NaMTiO_{2.2}S_{1.8}$. These two quantities show a strong correlation: the most active sample, M = Gd, also exhibited the highest $\Delta\sigma_{max}$. Notably, a similar correlation was obtained when comparing $\Delta\sigma_{max}$ at the excitation wavelength giving the maximum TRMC response (Fig. S19), confirming that this trend is not specific to the 500 nm excitation. Additionally, the apparent quantum yields (AQYs) (excitation at 525 nm) of $NaGdTiO_{2.2}S_{1.8}$ (highest $\Delta\sigma_{max}$) (1.2 %) was approximately three times higher than that of $NaEuTiO_{2.2}S_{1.8}$ (lowest $\Delta\sigma_{max}$) (0.48 %), further supporting the strong correlation. The lanthanoid-dependent variation in photoconductivity is likely associated with the energy levels of their empty f-orbitals. Because f-orbitals interact only weakly with the surrounding environment and remain essentially localized, the empty f-orbital levels are expected to deepen in the order Gd < Pr < Nd < Sm < Eu, as suggested in previous reports.[29,30] Deeper f-orbitals, located energetically below the CBM, act as electron-trapping sites, thereby enhancing charge carrier recombination. In fact, M = Eu, which possesses the deepest empty f-orbital, exhibited the lowest $\Delta\sigma_{max}$ and the lowest amount of H_2 evolution. Notably, the fact that M = Gd exhibited the largest interlayer hydration amount (*i.e.*, a greater availability of reactants) may also contribute to its highest photocatalytic activity (Fig. S11). Taken together, $NaGdTiO_{2.2}S_{1.8}$ exhibits superior carrier-transport properties originating from the relatively shallow empty f-orbitals of Gd, thereby enabling Ni(in)/$NaGdTiO_{2.2}S_{1.8}$ to achieve higher H_2 evolution activity than the other lanthanoid analogues.

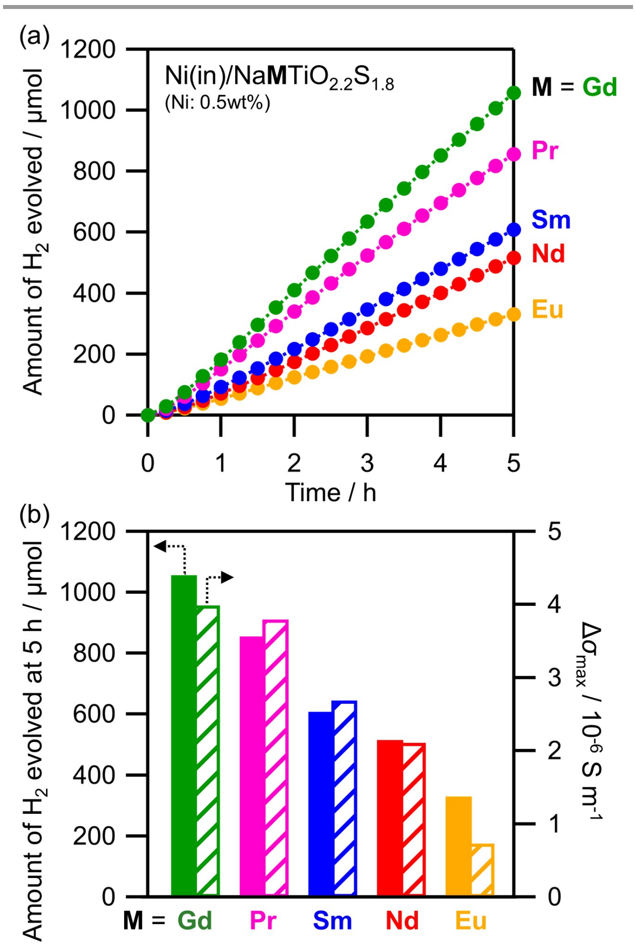

Fig. 4 (a) Time courses of photocatalytic H_2 evolution on Ni(in)/$NaMTiO_{2.2}S_{1.8}$ (M = Pr, Nd, Sm, Eu, and Gd) from water with electron donors (S^{2-} and SO_3^{2-}) under visible light (400 < λ < 800 nm). (b) Amount of H_2 evolution at 5 h on Ni(in)/$NaMTiO_{2.2}S_{1.8}$ (M = La, Pr, Nd, Sm, Eu, and Gd) (solid bars) and $\Delta\sigma_{max}$ obtained from TRMC measurements (λ_{ex} = 500 nm, $I_0 = 4.6 \times 10^{15}$ photons cm^{-2} $pulse^{-1}$) for $NaMTiO_{2.2}S_{1.8}$.

To verify the intercalation of Ni species into the interlayer space *via* the ion-exchange method described above, we first increased the amount of Ni introduced into the interlayer of $NaGdTiO_{2.2}S_{1.8}$ by adjusting the Na:Ni molar ratio to 2:1 (Fig. S20). The XRD pattern exhibited an overall peak shift, particularly the (001) peak, toward lower angles relative to the original positions. Upon vacuum drying, the peaks shifted toward higher angles, indicating the presence of interlayer water molecules. Moreover, after drying, the peaks shifted to higher angles compared with the original $NaGdTiO_{2.2}S_{1.8}$, suggesting the contraction of the *c*-axis lattice parameter and Na^+ was partially replaced by the smaller Ni^{2+}. EDX analysis also confirmed that Ni was uniformly distributed within the sample (Fig. S21a). For comparison, ion-exchange experiments were also conducted using bulky $[Ni(en)_3]^{2+}$ (en = ethylenediamine) and anionic $[Ni(CN)_4]^{2-}$ under the same conditions: $[Ni(en)_3]^{2+}$ was prepared by adding the chelating agent en to a $Ni(NO_3)_2$ solution (its formation was confirmed by UV-visible spectroscopy,[31] Fig. S22), whereas $[Ni(CN)_4]^{2-}$ was obtained simply by dissolving $K_2[Ni(CN)_4]$ in water. However, no peak shift was observed after these treatments (Fig. S20), and EDX analysis detected no Ni incorporation (Figs. S21b, c). These results indicate that ion-exchange proceeds only when Ni is present as the aqua complex $[Ni(H_2O)_x]^{2+}$, whereas bulky $[Ni(en)_3]^{2+}$ and anionic $[Ni(CN)_4]^{2-}$ cannot be accommodated in the interlayer space.

Fig. 5 shows the high-angle annular dark field scanning transmission electron microscopy (HAADF-STEM) images of Ni(in)/$NaGdTiO_{2.2}S_{1.8}$ prepared with Ni loadings of 0.5 wt% (Na:Ni = 1:0.003 molar ratio) and 5 wt% (Na:Ni = 1:0.03 molar ratio). At 0.5 wt%, successful loading of Ni species was suggested by the decrease in Ni concentration in the ion-exchange solution after treatment (Fig. S23). Although a slight local increase in brightness can be discerned within the Na layer between adjacent Gd layers, the presence of intercalated Ni cannot be unambiguously confirmed (Fig. 5a). At 5 wt% the brightness in the same region increases noticeably, accompanied by local bending of the layered structure, suggesting that more Ni intercalation induces the distortion of the stacking (Fig. 5b). Additionally, in the annular dark field

View Article Online
DOI: 10.1039/D6SC02806C

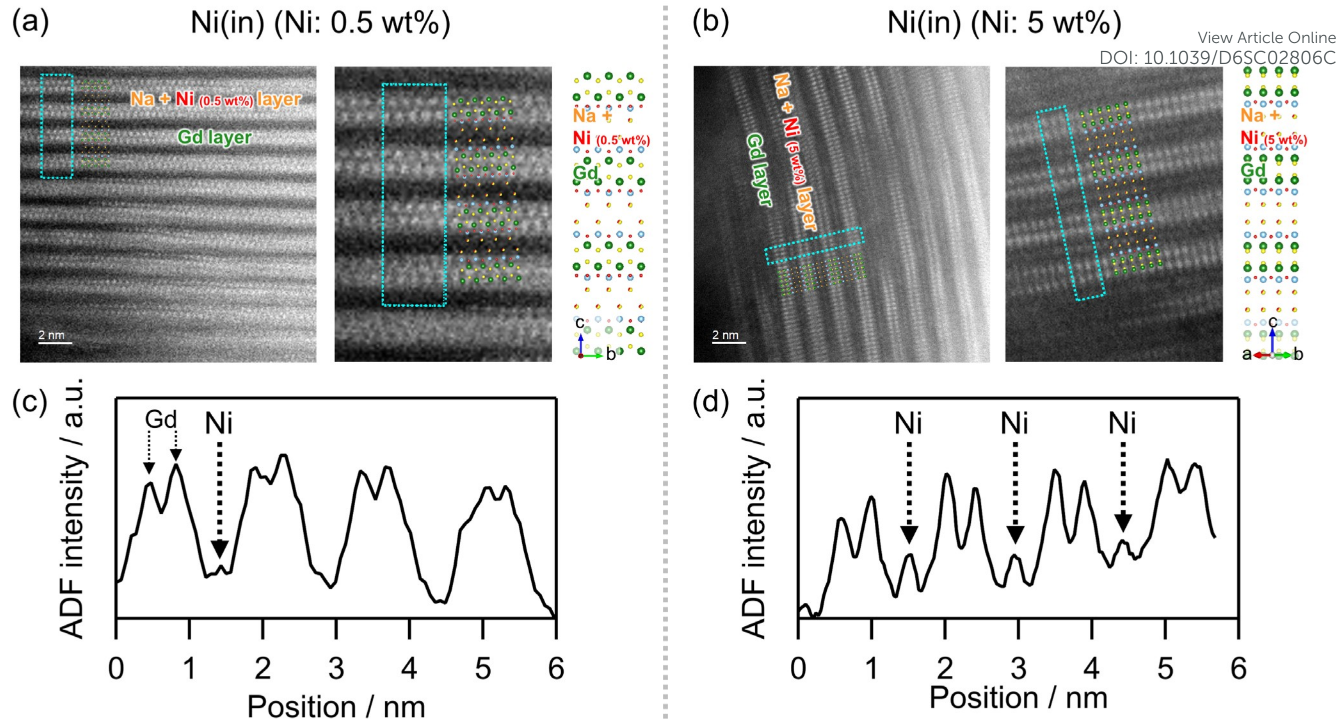

Fig. 5 HAADF-STEM images and corresponding ADF line profiles of Ni(in)/$NaGdTiO_{2.2}S_{1.8}$ with Ni loadings of (a, c) 0.5 wt% and (b, d) 5 wt% (as Ni metal). The crystal structure of $NaGdTiO_{2.2}S_{1.8}$ is projected along the (a) [100] and (b) [110] directions.

(ADF) line profiles of both samples, a slight intensity increase attributable to Ni incorporation was observed between the Gd layers, becoming more pronounced at 5 wt% (Figs. 5c, d). Furthermore, EDX analysis confirms that Ni species are uniformly intercalated at 5 wt%, while a smaller yet still uniformly distributed amount of Ni is also detected at 0.5 wt% (Fig. S24). Taken together with the Ni K-edge X-ray absorption fine structure (XAFS) analysis (Fig. S25), these results demonstrate that the present method successfully introduces $[Ni(H_2O)_x]^{2+}$ species into the interlayer of $NaMTiO_{2.2}S_{1.8}$ *via* ion-exchange with interlayer Na^+.

To verify that the interlayer could serve as an active site (*i.e.*, Ni site) for water reduction, the photocatalytic activities of Ni(in)/$NaGdTiO_{2.2}S_{1.8}$, with Ni species intercalated in the interlayer, were compared with those of bare $NaGdTiO_{2.2}S_{1.8}$ and Ni(out)/$NaGdTiO_{2.2}S_{1.8}$, where Ni species were loaded on the particle surface (Fig. 6a). First, the Ni loading amount in the interlayer was optimized, with 0.5 wt% Ni loading exhibiting the highest activity (Fig. S26). Next, the conditions for surface loading Ni species were optimized using $[Ni(en)_3]^{2+}$ or $[Ni(CN)_4]^{2-}$ as precursors. Between these, Ni(out)/$NaGdTiO_{2.2}S_{1.8}$, prepared using $[Ni(CN)_4]^{2-}$ as the precursor and calcined under an Ar flow at 773 K after impregnation, exhibited the highest activity (Figs. S27–S29). The photocatalytic activities of the M/$NaGdTiO_{2.2}S_{1.8}$ samples under these optimized conditions (M = Ni(in), Ni(out)) and $NaGdTiO_{2.2}S_{1.8}$ (bare) are summarized in Fig. 6a and Table S9. $NaGdTiO_{2.2}S_{1.8}$ loaded with Ni species in the interlayer demonstrated significantly higher activity than that loaded on the surface. Additionally, the photocatalytic activity of Ni(in)/$NaGdTiO_{2.2}S_{1.8}$ is three times higher than that of surface Rh-loaded samples prepared by the conventional photodeposition method (1wt% Rh as Rh metal, optimized in the range of 0.5–5 wt%) (Fig. S30). This remarkable enhancement strongly suggests that utilizing the interlayer (*i.e.*, Ni site) as a water reduction site allows efficient use of electrons within the particle (Fig. 6d).

To investigate the chemical state of interlayer Ni species and the electron transfer from the photocatalyst to them, XAFS and TRMC measurements were conducted (Figs. 6b, c). To compare the active Ni species under the photocatalytic conditions, XAFS measurements were performed on Ni(in)/$NaGdTiO_{2.2}S_{1.8}$ and Ni(out)/$NaGdTiO_{2.2}S_{1.8}$ after the photocatalytic reaction (Figs. 6b and S31). The X-ray absorption near edge structure (XANES) spectra of all these samples resembled that of $Ni(OH)_2$, and similar results were obtained from the Fourier-transformed extended XAFS (EXAFS) spectra. These results indicate that Ni species are predominantly present in a divalent state coordinated by oxygen, regardless of whether they are located in the interlayer or on the particle surface. Fig. 6c shows TRMC signals for bare $NaGdTiO_{2.2}S_{1.8}$, Ni(in)/$NaGdTiO_{2.2}S_{1.8}$, and Ni(out)/$NaGdTiO_{2.2}S_{1.8}$. In n-type semiconductors like $NaGdTiO_{2.2}S_{1.8}$, the TRMC signal mainly reflects the behaviour of photoexcited electrons. The reduced signal for Ni(in) compared with the bare sample indicates that interlayer Ni species effectively captured electrons. More importantly, compared with surface-loaded Ni species (Ni(out)), the TRMC signal of Ni(in) decreased even more significantly, demonstrating more efficient electron capture, despite having a similar chemical state. This observation suggests that the presence of Ni species in the interlayer allows for electron capture not only near the

View Article Online
DOI: 10.1039/D6SC02806C

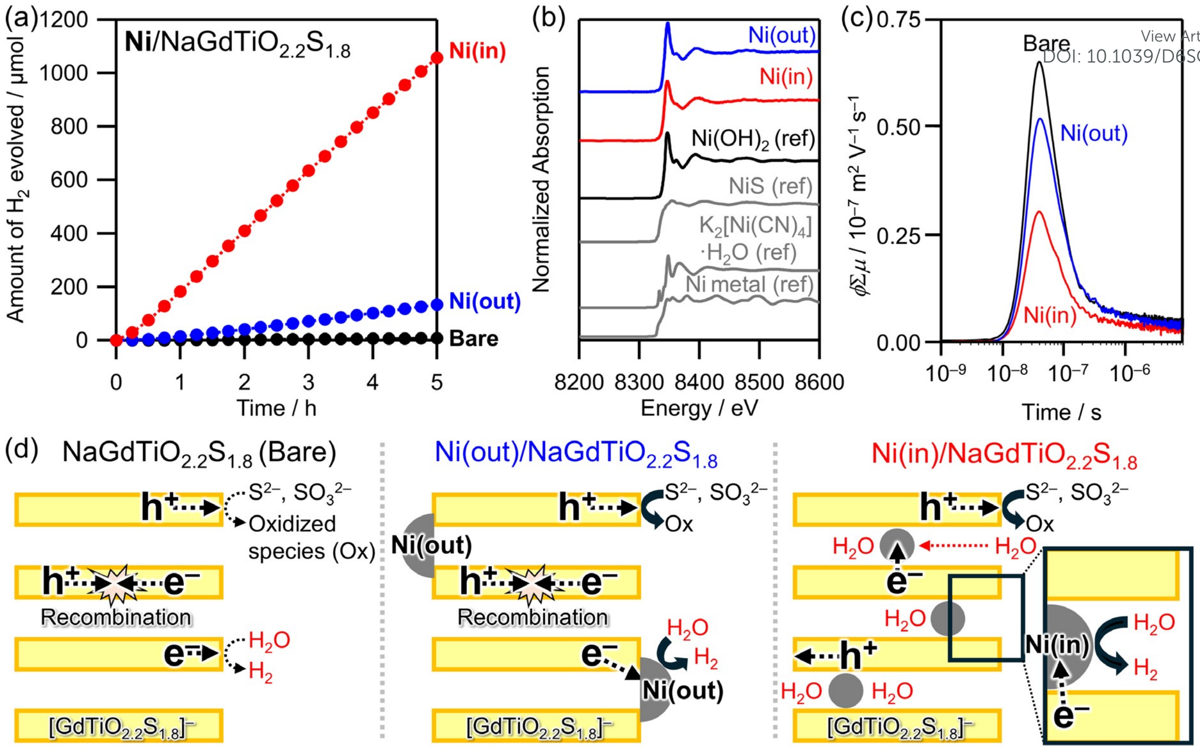

Fig. 6 (a) Time courses of photocatalytic H_2 evolution on $NaGdTiO_{2.2}S_{1.8}$ (bare) and $Ni/NaGdTiO_{2.2}S_{1.8}$ (Ni(in) and Ni(out)) from water with electron donors (S^{2-} and SO_3^{2-}) under visible light ($400 < \lambda < 800$ nm). (b) Ni K-edge XANES spectra of $Ni/NaGdTiO_{2.2}S_{1.8}$ after the photocatalytic reaction along with the spectra of reference samples. (c) TRMC transients (λ_{ex} = 355 nm, $I_0 = 4.6 \times 10^{15}$ photons cm^{-2} pulse^{-1}) of $Ni/NaGdTiO_{2.2}S_{1.8}$ after the photocatalytic reaction compared with bare $NaGdTiO_{2.2}S_{1.8}$. (d) Schematic illustration of photocatalytic H_2 evolution.

particle surface but also within the interior of the particle (Fig. 6d).

Finally, the effect of particle size on the utilization of the interlayer as reaction sites was investigated. $NaGdTiO_{2.2}S_{1.8}$ was synthesized *via* SSR at 1023, 1123, and 1223 K; XRD confirmed that the main phase was obtained at all three temperatures (Fig. S32). SEM observations revealed that the samples prepared at 1023 and 1123 K consisted of relatively small particles, whereas pronounced particle coarsening occurred at 1223 K (Fig. S33). After ion-exchange with $[Ni(H_2O)_x]^{2+}$, the H_2 evolution activity of $Ni(in)/NaGdTiO_{2.2}S_{1.8}$ prepared at 1023 K was significantly higher than that synthesized at 1223 K and slightly higher than that prepared at 1123 K (Fig. S34a). In contrast, the activities of $Rh(out)/NaGdTiO_{2.2}S_{1.8}$ were comparable across 1023–1223 K, with the highest activity observed at 1123 K (Fig. S34b). These results suggest that smaller particle sizes can promote more effective utilization of the interlayer as reaction sites by enhancing reactant/product transport into the interlayer. Further particle downsizing is expected to enhance the activity of the present system. Importantly, such control over particle size is difficult to realize by the previous H_2S-based synthesis at a high temperature.

Conclusions

In conclusion, this study presents the first demonstration of visible-light-driven hydrogen evolution by exploiting the interlayer space as photocatalytic reaction sites through particle design of the layered oxysulfide $NaMTiO_{2.2}S_{1.8}$ (lanthanoid). Nearly single-phase $NaMTiO_{2.2}S_{1.8}$ (M = Nd, Sm; newly including La, Pr, Eu, and Gd) was successfully synthesized *via* SSR at 1023 K without using H_2S, yielding submicrometer particles much smaller than those obtained by the previous H_2S-based method. STEM observations combined with XAFS measurements confirmed that Ni species were introduced into the interlayer *via* ion exchange as $[Ni(H_2O)_x]^{2+}$. The H_2 evolution activity of the interlayer-Ni-loaded samples increased in the order Eu < Nd < Sm < Pr < Gd, which correlated well with their TRMC signals, indicating that carrier transport and accessibility to the reaction sites play key roles, consistent with reduced electron trapping at lanthanoid sites (*i.e.*, the relatively shallow empty 4f levels of Gd). Interlayer-Ni-loaded $NaGdTiO_{2.2}S_{1.8}$ exhibited significantly higher H_2 evolution activity than the surface-loaded counterparts, owing to more efficient electron transfer to interlayer Ni species, as confirmed by TRMC measurements. Overall, this study establishes the interlayer of a layered oxysulfide photocatalyst as an effective water reduction site that is spatially separated from the electron-donor oxidation at the outer surface. This design strategy is expected to be applicable to more advanced photocatalytic reactions that require high selectivity toward the desired transformation.

View Article Online
DOI: 10.1039/D6SC02806C

Experimental section

Materials.

Na_2CO_3 (99.8 %), La_2O_3 (99.99 %), Nd_2O_3 (99.9 %), Sm_2O_3 (99.9 %), Eu_2O_3 (99.9 %), Gd_2O_3 (99.9 %), Y_2O_3 (99.99 %), TiO_2 (98.5 %), 0.5 M H_2SO_4 aqueous solution (aq.), $RhCl_3\cdot3H_2O$ (95.0-102.0 %), Na_2S (98.0 %), Na_2SO_3 (97.0 %), Na_2SO_4 (99.0 %), $AgNO_3$ (99.8 %), $Ni(NO_3)_2\cdot6H_2O$ (98.0 %), $K_2[Ni(CN)_4]\cdot H_2O$ (80.0 %), and ethylenediamine (en) (99.0 %) were purchased from FUJIFILM Wako Pure Chemical Corporation. Pr_2O_3 (99.9 %), Nd_2S_3 (99.9 %), and TiS_2 (99.9 %) were purchased from Kojundo Chemical Laboratory Co., Ltd. $[Ni(en)_3](NO_3)_2$ precursor was prepared by adding en into an aqueous $Ni(NO_3)_2$ solution at a molar ratio of Ni:en = 1:6.

Sample preparation.

$NaMTiO_{2.2}S_{1.8}$ samples (M = La, Pr, Nd, Sm, Eu, Gd, and Y) were synthesized *via* an SSR from a mixture of Na_2CO_3, M_2O_3, and TiS_2 with a molar ratio of Na:M:Ti = 1:1:1. The mixture was placed in an alumina tube, which was then inserted into an evacuated quartz tube and calcined at 723–1323 K for 24 h. (723–1323 K for M = Nd; 1023–1223 K for M = Gd; 1023 K for M = La, Pr, Sm, Eu, and Y).

For the ion-exchange of $NaMTiO_{2.2}S_{1.8}$, the synthesized powder was immersed in an aqueous H_2SO_4 solution (pH = 2.5) in the dark at room temperature for 1 h. After immersion, the obtained samples were collected by filtration and dried naturally.

For loading $[Ni(H_2O)_x]^{2+}$ (0.1–5 wt% as Ni metal; typically 0.5 wt%) into the interlayer of $NaMTiO_{2.2}S_{1.8}$, the oxysulfide powder was immersed in an aqueous $Ni(NO_3)_2$ solution in the dark at room temperature for 24 h. The resulting samples were collected by filtration, dried naturally, and denoted as Ni(in)/$NaMTiO_{2.2}S_{1.8}$. For comparison, Ni was loaded onto the surface $NaMTiO_{2.2}S_{1.8}$ (*i.e.*, outside the interlayer) *via* an impregnation method using $K_2[Ni(CN)_4]$ as the Ni precursor (0.5 wt% as Ni metal). The impregnated powders were then heated at 773 K for 1 h under an Ar flow (20 mL/min), yielding Ni(out)/$NaMTiO_{2.2}S_{1.8}$.

Characterization.

Powder XRD (MiniFlex II, Rigaku, X-ray source: CuKα), UV-visible diffuse reflectance spectroscopy (V–650, JASCO), SEM (NVision 40, Carl Zeiss-SIINT) and STEM (JEOL, JEM-ARM200CF) equipped with EDX were used to characterize the samples. Synchrotron XRD (SXRD; BL02B2, SPring-8, Japan, λ = 0.4139319 Å) patterns were collected at room temperature. Indexing of the SXRD patterns and Rietveld refinement were conducted using JANA2006.[32] The VESTA program was used to construct the crystal structures.[33] XAFS measurements were carried out at the BL12C beamline of the Photon Factory (High Energy Accelerator Research Organization, Tsukuba, Japan). The X-ray energy was varied by using a Si(111) double-crystal monochromator. Reference samples were diluted in boron nitride, compressed to form pellets, and measured in transmission mode. Cocatalyst-loaded samples were measured in a fluorescence mode using a multichannel solid-state detector.

Electrochemical measurement.

MS plots were recorded using an electrochemical analyzer (VersaSTAT 4, Princeton Applied Research) with an amplitude of 10 mV and a frequency of 1000 Hz. The three-electrode cell consisted of a Pt wire counter electrode and an Ag/AgCl reference electrode in a phosphate-buffered solution (0.1 M, pH = 12.0). The working electrode was prepared using the squeegee method: a particulate sample with a small amount of water was coated on a fluorine-doped tin oxide conductive substrate and dried overnight at room temperature.

TRMC measurements.

TRMC measurements were carried out using the third harmonic generation (THG at 355 nm, 4.6 × 10^{15} photons cm^{-2} $pulse^{-1}$) of an Nd:YAG laser (Continuum Inc., Surelite II, 5–8 ns pulse duration, 10 Hz) or the visible light (440–660 nm) from an optical parametric oscillator (Continuum Inc., Panther) seeded by the Nd:YAG laser (Surelite II). The resonant frequency and microwave power were set to ~9.1 GHz (X-band) and 3 mW, respectively. The powdered samples were fixed to quartz substrates using optically clear adhesive tape (the tape does not interfere with any TRMC signal). The photoconductivity was measured along the direction horizontal to the substrate, unless otherwise stated. The photoconductivity ($\Delta\sigma$) was calculated using the following formula: $\Delta\sigma = \Delta P_r/(AP_r)$, where ΔP_r, A, and P_r are the changes in the reflected microwave power, sensitivity factor, and power of the reflected microwave, respectively. The photoconductivity ($\Delta\sigma$) was converted to the product of the quantum yield (φ) and the sum of charge carrier mobilities $\Sigma\mu$ (= $\mu_+ + \mu_-$) by applying the following formula: $\varphi\Sigma\mu = \Delta\sigma\ (eI_0F_{light})^{-1}$, where e, I_0, and F_{light} are the unit charge of a single electron, the incident photon density of the excitation laser, and a correction (or filling) factor, respectively.

Photocatalytic reactions.

Photocatalytic reactions were carried out in a Pyrex glass reactor under an Ar flow (20 mL min^{-1}). The quantity of evolved gases was determined using an online gas chromatograph (GC 3210D, GL Sciences, thermal conductivity detector, column packing: 5 Å molecular sieves, and Ar carrier gas). For the photocatalytic H_2 evolution, the photocatalyst powders (0.05 g) were suspended in 180 mL of an aqueous Na_2S/Na_2SO_3 solution (10 mM each) containing Na_2SO_4 (0.5 M). Ni was loaded onto the photocatalyst *via* the method described above. Rh was loaded onto the photocatalyst surface *via in situ* photodeposition using $RhCl_3\cdot3H_2O$ (0.5–5 wt% as Rh metal), denoted as Rh(out)/$NaMTiO_{2.2}S_{1.8}$. The photocatalysts were irradiated with visible light (λ > 400 nm) using a cutoff filter (HOYA; L42) from a 300 W Xe-arc lamp (PerkinElmer, Cermax PE300BF). AQY for H_2 evolution was measured using an LED lamp (CL-H1-525-7-1-B) (Asahi Spectra Co.); the AQY value was estimated as follows.

$$\text{AQY (\%)} = (2 \times R/I) \times 100$$

R and I represent the H_2 evolution rate and the rate of incident photons, respectively. The total number of incident photons (67

View Article Online
DOI: 10.1039/D6SC02806C

mW at 525 nm) was measured using an optical power meter (Hiokioptical power meter 3664).

Conflicts of interest

There are no conflicts to declare.

Data availability

All data are available in the main manuscript and the Supporting Information. XRD patterns, EDX, SEM images, crystal structures, structural analysis from Rietveld refinement, TRMC signals, UV-visible diffuse reflectance spectra, MS plots, TG-DTA profiles, absorption spectra, XAFS spectra and photocatalytic activities. See DOI: 10.1039/x0xx00000x.

Acknowledgements

This study was supported by JSPS KAKENHI (Grants-in-Aid for Scientific Research (A) JP20H00398 and (B) JP23H02061, JP26K01604), JST SPRING (JPMJSP2110) and JST PRESTO (JPMJPR25M8). This study was supported by Samco Foundation. The authors would like to acknowledge Dr. Rie Haruki, High Energy Accelerator Research Organization (KEK), for helping with XAFS measurements. We are also grateful to Mr. Takaaki Toriyama of Kyushu University for his support with the STEM analysis.

References

1 K. Takada, H. Sakurai, E. Takayama-Muromachi, F. Izumi, R. A. Dilanian and T. Sasaki, *Nature*, 2003, **422**, 53–55.
2 J. Qian, L. Liu, J. Yang, S. Li, X. Wang, H. L. Zhuang and Y. Lu, *Nat. Commun.*, 2018, **9**, 4918.
3 D. Neiner, L. Spinu, V. Golub and J. B. Wiley, *Chem. Mater.*, 2006, **18**, 518–524.
4 H. Yim, S. Y. Yoo, Y. H. Kim, K. H. Chae, Y.-H. Kim, S. K. Kim, S.-H. Baek, C.-H. Lee and J.-W. Choi, *Chem. Mater.*, 2021, **33**, 8685–8692.
5 S. Sekizaki, M. Osada and K. Nagashio, *Nanoscale*, 2017, **9**, 6471–6477.
6 Y. Okamoto, S. Ida, J. Hyodo, H. Hagiwara and T. Ishihara, *J. Am. Chem. Soc.*, 2011, **133**, 18034–18037.
7 T. Oshima, S. Nishioka, Y. Kikuchi, S. Hirai, K. Yanagisawa, M. Eguchi, Y. Miseki, T. Yokoi, T. Yui, K. Kimoto, K. Sayama, O. Ishitani, T. E. Mallouk and K. Maeda, *J. Am. Chem. Soc.*, 2020, **142**, 8412–8420.
8 T. Takata, K. Shinohara, A. Tanaka, M. Hara, J. N. Kondo and K. Domen, *J. Photochem. Photobiol. A: Chem.*, 1997, **106**, 45–49.
9 A. Kudo, K. Sayama, A. Tanaka, K. Asakura, K. Domen, K. Maruya and T. Onishi, *J. Catal.*, 1989, **120**, 337–352.
10 T. Takata, Y. Furumi, K. Shinohara, A. Tanaka, M. Hara, J. N. Kondo and K. Domen, *Chem. Mater.*, 1997, **9**, 1063–1064.
11 K. Sayama, A. Tanaka, K. Domen, K. Maruya and T. Onishi, *J. Catal.*, 1990, **124**, 541–547.
12 J. B. Goodenough and Y. Kim, *Chem. Mater.*, 2010, **22**, 587–603.
13 B. V. R. Reddy, R. Ravikumar, C. Nithya and S. Gopukumar, *J. Mater. Chem. A*, 2015, **3**, 18059–18063.
14 Y.-J. Guo, R.-X. Jin, M. Fan, W.-P. Wang, S. Xin, L.-J. Wan and Y.-G. Guo, *Chem. Soc. Rev.*, 2024, **53**, 7828–7874.
15 T. W. Kim, I. Y. Kim, T. S. Jung, C. H. Ko and S. Hwang, *Adv. Funct. Mater.*, 2013, **23**, 4377–4385.
16 S. Radha and A. Navrotsky, *J. Phys. Chem. C*, 2014, **118**, 29836–29844.
17 H. B. M. Sidek, Y. K. Jo, I. Y. Kim and S.-J. Hwang, *J. Phys. Chem. C*, 2016, **120**, 23421–23429.
18 R. Yu, C. Wang, H. Duan, M. Jiang, A. Zhang, A. Fraser, J. Zuo, Y. Wu, Y. Sun, Y. Zhao, J. Liang, J. Fu, S. Deng, Z. Ren, G. Li, H. Huang, R. Li, N. Chen, J. Wang, X. Li, C. V. Singh and X. Sun, *Adv. Mater.*, 2023, **35**, e2207234.
19 H. Takahashi, T. Takeguchi, T. Yamanaka, T. Kyomen, M. Hanaya and W. Ueda, *Electrochem. Soc. Trans.*, 2010, **33**, 1861–1866.
20 D. Zhao, K. Shi, Y. Lu, T. Zhang, H. Jin, Z. Yan and J. Chen, *Sci. China Chem.*, 2025, 1–16.
21 K. Sayama, K. Yase, H. Arakawa, K. Asakura, A. Tanaka, K. Domen and T. Onishi, *J. Photochem. Photobiol. A: Chem.*, 1998, **114**, 125–135.
22 R. Abe, K. Shinmei, N. Koumura, K. Hara and B. Ohtani, *J. Am. Chem. Soc.*, 2013, **135**, 16872–16884.
23 M. Machida, K. Miyazaki, S. Matsushima and M. Arai, *J. Mater. Chem.*, 2003, **13**, 1433–1437.
24 D. E. Scaife, *Sol. Energy*, 1980, **25**, 41–54.
25 Y. Ishii, H. Suzuki, D. Kato, O. Tomita, A. Nakada and R. Abe, *Chem. Sci.*, 2025, **16**, 16534–16541.
26 A. Saeki, M. Tsuji and S. Seki, *Adv. Energy Mater.*, 2011, **1**, 661–669.
27 H. Suzuki, S. Kanno, M. Hada, R. Abe and A. Saeki, *Chem. Mater.*, 2020, **32**, 4166–4173.
28 N. Kinomura, N. Kumada and F. Muto, *J. Chem. Soc., Dalton Trans.*, 1985, 2349–2351.
29 P. Dorenbos, *J. Phys.: Condens. Matter*, 2003, **15**, 8417.
30 A. J. J. Bos, P. Dorenbos, A. Bessière and B. Viana, *Radiat. Meas.*, 2008, **43**, 222–226.
31 H. B. Mark. Jr., *J. Electroanal. Chem.*, 1964, **8**, 253–261.
32 Petricek, D. M. and P. L., *Z. Kristallogr.*, 2014, **229**, 345–352.
33 K. Momma and F. Izumi, *J. Appl. Crystallogr.*, 2011, **44**, 1272–1276.

View Article Online
DOI: 10.1039/D6SC02806C

The data supporting this article have been included as part of the Supplementary Information.